Detection capabilities of the Athena X-IFU for the warm-hot intergalactic medium using gamma-ray burst X-ray afterglows

Sarah Walsh[1], Sheila McBreen[1], Antonio Martin-Carrillo[1], Thomas Dauser[2], Nastasha Wijers[3], Jörn Wilms[2], Joop Schaye[3], and Didier Barret[4]

[1] School of Physics, University College Dublin, Dublin 4, Ireland. e-mail: `sarah.walsh.2@ucdconnect.ie`
[2] Remeis Observatory & ECAP, Universität Erlangen-Nürnberg, Sternwartstr. 7, 96049 Bamberg, Germany
[3] Leiden Observatory, Leiden University, PO Box 9513, NL-2300 RA Leiden, the Netherlands
[4] Université de Toulouse, CNRS, Institut de Recherche en Astrophysique et Planétologie, 9 Avenue du colonel Roche, BP 44346, 31028 Toulouse Cedex 4, France

ABSTRACT

At low redshifts, the observed baryonic density falls far short of the total number of baryons predicted. Cosmological simulations suggest that these baryons reside in filamentary gas structures, known as the warm-hot intergalactic medium (WHIM). As a result of the high temperatures of these filaments, the matter is highly ionised such that it absorbs and emits far-UV and soft X-ray photons. *Athena*, the proposed European Space Agency X-ray observatory, aims to detect the 'missing' baryons in the WHIM up to redshifts of $z = 1$ through absorption in active galactic nuclei and gamma-ray burst afterglow spectra, allowing for the study of the evolution of these large-scale structures of the Universe. This work simulates WHIM filaments in the spectra of GRB X-ray afterglows with *Athena* using the SImulation of X-ray TElescopes (SIXTE) framework. We investigate the feasibility of their detection with the X-IFU instrument, through O VII ($E = 573$ eV) and O VIII ($E = 674$ eV) absorption features, for a range of equivalent widths imprinted onto GRB afterglow spectra of observed starting fluxes ranging between 10^{-12} and 10^{-10} erg cm^{-2} s^{-1}, in the 0.3–10 keV energy band. The analyses of X-IFU spectra by blind line search show that *Athena* will be able to detect O VII-O VIII absorption pairs with $EW_{O\,VII} > 0.13$ eV and $EW_{O\,VIII} > 0.09$ eV for afterglows with $F > 2 \times 10^{-11}$ erg cm^{-2} s^{-1}. This allows for the detection of ≈ 45–137 O VII-O VIII absorbers during the four-year mission lifetime. The work shows that to obtain an O VII-O VIII detection of high statistical significance, the local hydrogen column density should be limited at $N_H < 8 \times 10^{20}$ cm^{-2}.

Key words. Gamma-ray burst: general - large-scale structure of Universe - X-rays: general - intergalactic medium - instrumentation: detectors

1. Introduction

Predictions from Big Bang nucleosynthesis (BBN; Cyburt et al. 2016, and references therein) combined with observations of the abundance of light elements (Burles & Tytler 1998), and the temperature fluctuations of the cosmic microwave background (CMB) taken independently (Spergel et al. 2003; Planck Collaboration et al. 2014), show that baryonic matter accounts for only $\approx 4\%$ of the total cosmic energy content. However, at the current epoch, the observed baryon density appears to be much lower (Fukugita et al. 1998), with studies showing only $\approx 60\%$ of these baryons are detected (Shull et al. 2012).

Cosmological hydrodynamic simulations, based on the ΛCDM model, predict that these 'missing' baryons reside in gaseous filamentary structures known as the warm-hot intergalactic medium (WHIM; Cen & Ostriker 1999; Davé et al. 2001; Cen & Ostriker 2006). These baryons are shock heated to temperatures of 10^5 K $< T < 10^7$ K as baryons in the diffuse intergalactic medium (IGM) accelerate towards sites of structure formation under the growing influence of gravitationally generated potential wells. Simulations predict that the WHIM accounts for approximately 30–60% of the baryonic mass at $z = 0$ (Davé et al. 2001; Tepper-García et al. 2012), making it the largest constituent of the IGM.

The high temperatures of these filaments result in the matter being highly ionised so that it absorbs and emits far-UV and soft X-ray photons. However, these WHIM filaments are of low column density and, therefore, produce a low signal intensity which makes them difficult to detect with the current instrumentation. In spite of this, the search for the missing baryons has continued and detections of extragalactic O VII and O VIII have been claimed (Nicastro et al. 2005) but they are often disputed (Kaastra et al. 2006; Williams et al. 2006; Rasmussen et al. 2007), of a single-line or low statistical significance (Nicastro et al. 2010; Bonamente et al. 2016), misidentifications of the WHIM (Nicastro et al. 2016), or they are local to the background source (Johnson et al. 2019). More recently, Nicastro et al. (2018), later updated by Nicastro (2018), reported the detection of two O VII absorption features at redshifts $z = 0.3551$ and $z = 0.4339$ along the sight-line towards blazar 1ES 1553+113 after a 1.75 Ms observation with the *XMM-Newton* reflection grating spectrometer. Johnson et al. (2019) conducted additional studies towards 1ES 1553+113, suggesting that the feature located at $z = 0.4339$ may not originate from the WHIM and is associated, rather, with the local environment of the blazar. A study by Kovács et al. (2019) quotes a 3.3σ detection of O VII towards H1821+643 from a stacked spectrum of *Chandra* observations with an 8 Ms total exposure. Ahoranta et al. (2020) performed spectral analysis of *Chandra* and *XMM-Newtown* observations at previously

determined FUV redshifts, yielding two X-ray line candidates of Ne IX Heα and O VIII Lyα at a combined significance of 3.9σ. In spite of the large observational efforts, only these few marginal detections have been achieved so far. The small equivalent widths of ≈ 0.07–0.42 eV (Branchini et al. 2009; Nicastro et al. 2018) from WHIM absorption features mean that high signal-to-noise ratio observations are required for their detection. This calls for an observatory with a large effective area, high energy resolution, and a low energy threshold in the soft X-ray energy band.

Selected as part of ESA's Cosmic Vision programme, *Athena* will study the evolution of large scale structure through the detection of WHIM filaments to trace the missing baryons in the local universe. *Athena* aims to measure the local cosmological baryon density in the WHIM to better than 10% and to constrain structure formation models in the low-density regime by measuring the redshift distribution and the physical parameters of 200 filaments against bright background sources. To achieve this, *Athena* will detect 200 filaments in the WHIM through absorption, 100 towards active galactic nuclei (AGN), and 100 towards bright gamma-ray burst (GRB) afterglows, up to redshifts of $z = 1$ (Kaastra et al. 2013). The WHIM can be detected by observing the absorption of highly ionised elements such as C, N, O, Ne, and possibly Fe (e.g. O VII, O VIII, Ne IX, Fe XVII). The strongest lines expected correspond to the H-like and He-like oxygen ions of the O VII 1s–2p X-ray resonance line (574 eV) and the unresolved O VIII 1s–2p X-ray doublet (653.5 eV, 653.7 eV). A bright X-ray background source such as an AGN (e.g. Padovani et al. 2017) or a GRB (e.g. Willingale & Mészáros 2017) can be used to detect the WHIM by producing absorption features in its energy spectra (Perna & Loeb 1998; Hellsten et al. 1998; Fiore et al. 2000). These sources provide a high probability of detection for the WHIM because they are sufficiently bright and distant to obtain a large statistical sample of lines. Bright AGN are common but are typically nearby, having an average redshift of $z \approx 0.8$ for flat-spectrum radio quasars (FRSQ) and $z \approx 0.3$ for BL-Lacs (Ackermann et al. 2011) and so, they probe relatively short lines of sight. Gamma-ray bursts occur at an average redshift of $z \approx 2$ (Evans et al. 2009) and have been detected out to redshifts of 9.4 (Cucchiara et al. 2011). This allows for the probing of long lines of sight and can potentially provide multi-filament detections in a single observation. In addition, GRBs occur at an approximate rate of 1 GRB per day, with *Fermi*-GBM detecting ≈ 250 per year with a ≈ 70% sky coverage (Bhat et al. 2016). Both sources provide similar fluences in the 0.3–10 keV energy range, but GRBs can provide this fluence in much shorter integration times. The challenge associated with the use of GRBs as background sources is their transient nature, emitting a considerable percentage of the soft X-ray photons within the first hour of their afterglow phase. Therefore, an instrument capable of having a high efficiency to react on target of opportunity (ToO) events is required to probe the WHIM with GRBs. In spite of this, GRBs should allow Athena to perform its science mission of tracing the missing baryons in GRB afterglow spectra throughout its four-year mission lifetime.

To achieve the goals set out by its science case, *Athena* will have two scientific instruments, the Wide Field Imager (WFI; Meidinger et al. 2017) and the X-ray Integral Field Unit (X-IFU; Barret et al. 2018). The WFI is a silicon-based detector using depleted field effect transistor (DEPFET) active pixel sensor technology that provides imaging in the 0.2–15 keV energy band over a wide field, simultaneously with spectrally- and time-resolved photon counting. The X-IFU is an array of transition edge sensors (TES), which provides spatially high resolution

spectroscopy over an energy range of 0.2–12 keV. The instrument has a field of view of 5′ equivalent diameter and will deliver X-ray spectra with a spectral resolution of 2.5 eV up to 7 keV. The high spectral resolution of the X-IFU makes it the prime instrument for the detection of the WHIM. Both instruments alternately share a moveable mirror system based on silicon pore optics with a focal length of 12 m and a large effective area of approximately 1.4 m² at an energy of 1 keV. The baseline configuration of the mirror consists of 15 rows of silicon pore optics. The *Athena* mirror assembly offers a defocusing capability, allowing for observations of the brightest X-ray sources of the sky, up to Crab-like intensities, by spreading the telescope point spread function over hundreds of pixels.

This work uses GRB afterglows as background sources for the detection of WHIM filaments. Gamma-ray bursts are the most luminous events known to occur in our Universe, consisting of energetic bursts of γ-rays from deep space. Early observations showed that the distribution of GRB duration was bimodal leading to the identification of short and long duration GRBs (e.g. Norris et al. 1984; Kouveliotou et al. 1993), where short GRBs have a typical duration (defined as T_{90}, the time over which 90 % of the total energy release in γ-rays is recorded) of $T_{90} < 2$ s while long GRBs have duration $T_{90} > 2$ s. Broad-band observations show that the two duration classes roughly correspond to two types of progenitor systems: long GRBs are related to deaths of massive stars (e.g. MacFadyen & Woosley 1999), while short GRBs are related to compact binary mergers (e.g. Blinnikov et al. 1984; Paczynski 1986).

Gamma-ray bursts consist of a prompt phase during which they can emit up to 10^{53} erg over a timescale of seconds and an afterglow phase which can last for days after the prompt phase and emits in energy bands from X-ray to radio. Studies of the GRB X-ray afterglow are performed with observatories such as the Neils Gehrels Swift Observatory (Gehrels et al. 2004), XMM-Newton (Jansen et al. 2001), the Chandra X-ray Observatory (Weisskopf et al. 2002), and INTEGRAL (Winkler et al. 2003), with their instruments regularly observing GRB sources tens of seconds after the trigger. The afterglow light curve of most GRBs can be described by a canonical light curve which includes five main temporal components each following a power-law decay of various decay indices (e.g. Zhang et al. 2006; Nousek et al. 2006; O'Brien et al. 2006; Evans et al. 2009).

Initial simulations of the WHIM detectability using GRB afterglows as a background source were implemented and detections were proved to be feasible using the 2 m² configuration of the *Athena* mirror (Brand et al. 2016; Brand 2016). This paper investigates the feasibility of detecting these missing baryons but with the current baseline (1.4 m² at 1 keV) mirror configuration. It advances the work of Brand et al. (2016) to determine the ability of the X-IFU to recover the characteristics of the WHIM absorption features and to determine the effect of Galactic absorption on the WHIM detection. It uses the current *Swift*-XRT GRB afterglow population and the results from EAGLE simulations (Schaye et al. 2015; Crain et al. 2015) to determine the number of O VII-O VIII absorption systems that may be detected by the X-IFU during its mission lifetime.

This paper is set out as follows. Section 2 describes the modelling of the GRB X-ray afterglow imprinted with WHIM absorption features and the simulations executed to create mock *Athena* X-IFU spectra. Section 3 discusses the data analysis method to search for WHIM absorbers in the simulated spectra. In Sect. 4.1, the probability of detecting the WHIM with the *Athena* X-IFU is presented for the defocused configuration of the mirror. Section 4.2 reports the equivalent width distribu-

tions that are obtained from the simulations and the ability of the X-IFU to reproduce the characteristics of the WHIM. The effect of the local hydrogen column density on the detection of WHIM absorption features at soft X-ray energies is investigated in Sect. 4.3. The results are discussed in Sect. 5 to assess the ability of *Athena* to discover the missing baryons of the WHIM. Finally, the findings of the paper are summarised in Sect. 6.

2. Simulating GRB afterglows

Specifically designed for the *Athena* X-IFU, *xifupipeline* executes the simulations of GRB spectra in the SImulation of X-ray TElescopes (SIXTE) framework[1] (Dauser et al. 2019). The simulations use the current $1.4\,m^2$ (at 1 keV) baseline configuration[2] of the *Athena* mirror. As the mirror offers a defocusing capability to maximise the photons collected by the X-IFU instrument during the observation of bright sources, the simulations are performed with the 35 mm defocused configuration. The main inputs for the pipeline are the SIMulation inPUT file (Schmid et al. 2013) which describes the light curve and spectrum of the observed source, the XML file which describes the X-IFU calorimeter, and the advanced XML which describes the grading scheme for detected photons. User-defined parameters are also input into the pipeline such as the pointing of the telescope in right ascension (α) and declination (Δ), the exposure time, and whether or not crosstalk between pixels is considered.

In all simulations, the exposure time was set to 50 ks, in accordance with the average exposure time allocated to the X-IFU for a given observation. Results for different exposure times can be obtained by scaling the flux of the results presented in this paper. Crosstalk was simulated between pixels and the grading of photons accepted was those of only high resolution where $\Delta E \leq 2.5$ eV.

The SIMPUT file contained one source modelled as a GRB afterglow by the input spectrum and light curve. The spectrum of the GRB afterglow was modelled by an absorbed power law comprising three main parts; an absorption function describing the Galactic absorption from the Milky Way galaxy, modelled by tbabs (Wilms et al. 2000); an absorption function describing the intrinsic absorption from the host galaxy of the GRB, modelled by ztbabs; and, a power-law, pegpwrlw, describing the GRB afterglow emission. The WHIM was modelled by two faint Gaussian absorption lines, zgauss, which were redshifted from the rest energy of the lines. The most prominent line expected is O VII and is located at a rest-frame energy of 574 eV, while the second line representing O VIII has a rest-frame energy of 654 eV. Both lines are assumed to originate from the same cosmic structure, and so, share the same redshift, z_{WHIM}. The parameters adopted for modelling the GRB afterglow spectrum and WHIM filaments are shown in Table 1.

A decaying power-law models the light curve of the GRB afterglow, which follows a relation between flux and time of $F \propto t^{\alpha}$, where $\alpha = -1.2$ is the power-law index (Margutti et al. 2013), in the relevant time range between two and 30 hours after the initial outburst occurred. The starting flux F_{start} of the GRB is defined as the observed flux of the GRB afterglow, measured in the 0.3–10 keV energy range, when the observation begins. This was varied from 10^{-12} to 10^{-10} erg cm^{-2} s^{-1} in accordance with fluxes of observed GRBs by the *Swift* X-ray observatory four hours after the initial burst. Located at varying redshifts, six WHIM lines of different equivalent widths from

the expected range of the WHIM were simulated for each flux. The redshift was varied randomly between $z_{WHIM} = 0.0$ and 0.5 to accommodate the search for local baryons within the *Athena* X-IFU energy band, while the equivalent widths were varied in the range $EW_{O VII} = 0.07$–0.42 eV (Branchini et al. 2009; Nicastro et al. 2018). For simplicity, the ratio between O VII and O VIII remained fixed for all input spectra and is given by the ratio of the ion oscillator strengths so that $EW_{O VIII} = 2/3 \cdot EW_{O VII}$. Fifty-one observations were simulated for each combination of equivalent width and GRB starting flux, with the redshift of the WHIM filament varying randomly in the given range. This provides a significant sample with a reasonable computation time.

The detection probability of two absorption features of Gaussian form can also be derived from Poissonian statistics. However, to verify the simulation method and the analysis method, and to create a simulation environment that incorporates the detector response, source light curves, and source spectra, the Monte Carlo simulations are performed to analyse the detectability of O VII and O VIII absorption features in GRB afterglow spectra. A comparison of both methods in shown in Appendix A.

3. Data analysis

3.1. Spectral fitting

The simulated spectra (e.g. Fig 1) were analysed in XSPEC v12.10 (Arnaud 1996). The optimal binning scheme of Kaastra & Bleeker (2016) with ftools ftgrouppha and the Cash statistic C (Cash 1979; Kaastra 2017) were used for the grouping and fitting of the spectral data.

The spectra were fitted in the energy range of 0.3–10 keV, which is within the energy range of the X-IFU. The model used for fitting the data was the same model that was used to generate the event data; an intrinsically absorbed power law, at the redshift of the GRB, with a Galactic absorption component and Gaussian absorption lines to represent the WHIM filaments. The absorption components were modelled with the tbabs and ztbabs components in XSPEC while wilm abundances (Wilms et al. 2000) and vern cross-sections (Verner et al. 1996) were used. The redshift of the GRB, and Galactic absorption were assumed to be known and were fixed during the fitting process, while all other parameters were free to vary. The WHIM lines were fitted by a blind line search as with real data the properties of the intergalactic gas and the distance at which it is located will not be known. The redshift range in which the blind line fitting process searches for absorption features was set to $0.0 \leq z_{WHIM} \leq 0.5$. The continuum parameters were initialised with the input model parameters while the energies of the absorption lines were set to their rest energies. The blind line search began at a redshift of $z_{WHIM} = 0$. At each iteration of the search the redshift was increased by $\Delta z_{WHIM} = 0.002$ and the corresponding fit statistic was determined. This was repeated for all redshift values in the search range, producing a list of fit statistic values, one for each redshift trial. From this list the redshift value of the best-fit model was determined by calculating the minimum C-value. This redshift value was taken to be the most significant line positions of the O VII and O VIII absorption features in the spectrum.

To assess the significance of these features, Monte Carlo simulations were performed, as described in Protassov et al. (2002), to eliminate the possibility that the absorption features were chance statistical fluctuations in the data. The best-fit model for the spectrum with no absorption features, that is, the continuum

Table 1: Spectral parameters used to model the GRB afterglow and WHIM filaments in all simulations

Model Component	Model Parameter	Value	References
Local Galaxy	Galactic Absorption	2×10^{20} cm^{-2}	
GRB Afterglow	Redshift, z_{GRB}	2.0	1
	Intrinsic Absorption	1×10^{22} cm^{-2}	1
	Photon Index	2.0	1
O VII Line at 574 eV	Redshift, z_{WHIM}	0.0–0.5	
	Equivalent Width, EW$_{O VII}$	0.07–0.42 eV	2, 3
	σ	0.1 eV ($b = 73$ km/s, $T \approx 5 \times 10^{6}$ K)	4
O VIII Line at 654 eV (2 line only)	Redshift, z_{WHIM}	0.0–0.5	
	Equivalent Width EW$_{O VIII}$	2/3 of O VII	4
	σ	0.1 eV ($b = 65$ km/s, $T \approx 4 \times 10^{6}$ K)	4

References. (1) Evans et al. (2009); (2) Branchini et al. (2009); (3) Nicastro et al. (2018); (4) Brand et al. (2016).
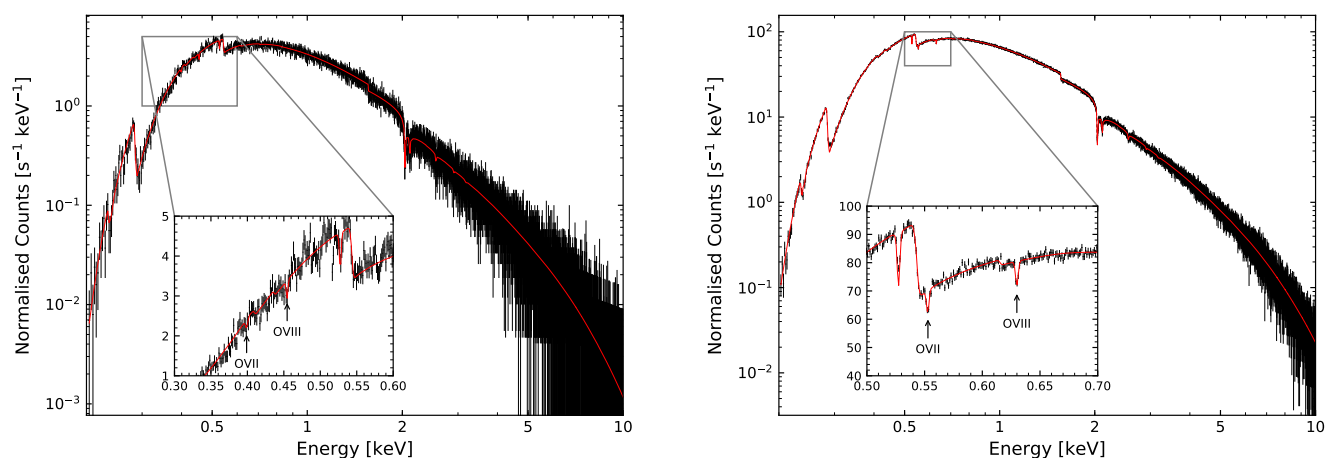

Fig. 1: 50 ks simulated X-IFU energy spectra of a GRB afterglow ($z_{GRB} = 2$) imprinted by O VII (EW$_{O VII}$ = 0.35 eV) and O VIII (EW$_{O VIII}$ = 0.23 eV) WHIM absorbers. Both spectra are binned using the optimal binning scheme of Kaastra & Bleeker (2016). *Left:* GRB absorbed starting flux 5×10^{-12} erg cm^{-1} s^{-1} and z_{WHIM} = 0.4388. *Right:* GRB absorbed starting flux 1×10^{-10} erg cm^{-1} s^{-1} and z_{WHIM} = 0.0382. The insets show the energy range around the WHIM absorption features. Note: The absorption feature located at ≈ 0.53 eV is the O resonance line of Galactic origin and is contained within the `tbabs` model component.

only[3], was assumed as the null hypothesis model and was simulated 100 times using XSPEC's `fakeit` command. Each simulated spectrum was then fit with the null hypothesis model to obtain the fit statistic. Two Gaussian absorption features, separated by a fixed energy, were simultaneously searched for using the same blind line fitting process as before in the same redshift range, producing a list of fit statistic values for each redshift trial in a simulated spectrum. The minimum C-value from the blind line search and the C-value from the continuum only fit for each of the simulated spectra were recorded. A distribution of the ΔC-values was obtained, where ΔC is the difference between the fit statistic of the continuum fit and the minimum fit statistic of the blind line search. The ΔC-values obtained from each simulated spectra create a distribution for which fitting statistical fluctuations in the spectrum improves the statistical fit of the continuum model. From this distribution, the ΔC-value that corresponds to a 90% significant detection for the original lines found in the data was determined. An original line is found to be significant if its measured ΔC-value is higher than the 90% significant ΔC-value from the distribution of the simulated set of spectra. Fi-

nally, it must be determined whether the features found by the significant detections are from the input WHIM lines. This was achieved by defining an additional margin of half the spectral energy resolution of the X-IFU, $\Delta z_{WHIM} = 1 \times 10^{-3}$ or ≈ 1.25 eV, on the energy of the detected absorption features relative to the known redshifted energy of the input lines. If an absorption feature is detected within the defined margin of their input energy, it is classed as a correct detection, otherwise, it is a false-alarm detection resulting from noise that has been fitted in the spectrum.

3.2. Detection probabilities of absorption features

All simulated observations of a given F_{start} and line equivalent width are combined to calculate the line detection probability by

$$P(\text{line found}, F_{start}, \text{EW}) = \frac{N(\text{sig. detection, correct } z_{WHIM}, F_{start}, \text{EW})}{N(F_{start}, \text{EW})},$$
(1)

where $N(F_{start}, \text{EW})$ is the total number of simulated observations for a given absorbed starting flux, F_{start} and equivalent

---

[3] `tbabs·ztbabs·pegpwrlw`

width, EW and N(significant detection, correct, z_{WHIM}, F_{start}, EW) is the total number of significant detections of $N(F_{\mathrm{start}}, \mathrm{EW})$ that were found at the correct WHIM redshift (Brand et al. 2016). Equation 1 provides the probability that a line or O VII-O VIII line pair is detected with a minimum significance of 90% and that the redshift it was detected at is within the energy margin defined in Sect. 3.1. The probability function can be used to determine the minimum absorbed starting flux of a GRB afterglow or the minimum number of spectral counts required to detect the absorption line or line pair of given strengths.

In addition to the probability of a line being detected, the false-alarm probability can be calculated. The false-alarm detection probability is the probability that an absorption feature has been determined to be significant to a minimum of a 90% threshold but lies outside the tolerated energy margin of the true value. It is determined by

$$P(\text{false-alarm}, F_{\mathrm{start}}, \mathrm{EW}) = \frac{N(\text{sig. detection, incorrect } z_{\mathrm{WHIM}}, F_{\mathrm{start}}, \mathrm{EW})}{N(\text{sig. detection}, F_{\mathrm{start}}, \mathrm{EW})} \quad (2)$$

Equation 2 gives an indication of the occurrence rate of selecting a noise feature within the spectra to be significant, over a real absorption feature, during the spectral analysis. The false-alarm probability is an important quantity because it could lead to a misinterpretation and over-estimate of the WHIM abundance, if not taken into account.

4. Results

4.1. Detection of O VII and O VIII in X-IFU spectra

Gamma-ray burst afterglow spectra containing a WHIM imprint of O VII and O VIII were simulated with the mirror in a 35 mm defocused configuration and were analysed using the method in Sect. 3. The results are shown in Fig. 2. The top panel shows the detection probability for observed starting fluxes of GRB afterglows in the range 10^{-12}–10^{-10} erg cm^{-2} s^{-1} in the 0.3–10 keV energy band and for line equivalent widths of $\mathrm{EW}_{\mathrm{O\,VII}} = 0.07$–$0.42$ eV, with O VIII having an equivalent width of $2/3 \cdot \mathrm{EW}_{\mathrm{O\,VII}}$.

The probability of detecting the WHIM by O VII-O VIII paired absorption features with at least a 90% significance increases with increasing afterglow flux and with increasing line equivalent widths. For the brightest GRB afterglow simulated of $F_{\mathrm{start}} = 10^{-10}$ erg cm^{-2} s^{-1}, there is at least an 80% chance of detecting an O VII-O VIII pair with $\mathrm{EW}_{\mathrm{O\,VII}} > 0.14$ eV. The weakest lines simulated with $\mathrm{EW}_{\mathrm{O\,VII}} = 0.07$ eV provide a $\sim 30\%$ chance of detection for the same starting flux. However, at the lowest afterglow flux of $F_{\mathrm{start}} = 10^{-12}$ erg cm^{-2} s^{-1}, none of the simulated lines are detected.

To obtain a 90% probability of detecting an O VII-O VIII absorption pair with at least a 90% significance, *Athena* should target GRB afterglows that have $F_{\mathrm{start}} > 3 \times 10^{-11}$ erg cm^{-2} s^{-1}. This limit allows the detection of absorbers with $\mathrm{EW}_{\mathrm{O\,VII}} > 0.2$ eV. To obtain a 50% probability of detecting an O VII-O VIII absorption feature with a minimum of 90% significance, an afterglow of $F_{\mathrm{start}} = 6$–20×10^{-12} erg cm^{-2} s^{-1} must be observed, limiting lines of $\mathrm{EW}_{\mathrm{O\,VII}} > 0.3$ eV. A starting flux of 5×10^{-11} erg cm^{-2} s^{-1} will be required from a GRB afterglow to have a 50% probability of detecting lines $\mathrm{EW}_{\mathrm{O\,VII}} > 0.15$ eV. The weakest absorber of 0.07 eV requires $F_{\mathrm{start}} = 8 \times 10^{-11}$ erg cm^{-2} s^{-1} during a 50 ks exposure to obtain a 20% probability of detecting absorption features with a 90% significance. These starting flux and equivalent width limits for 90%, 50%, and 20% detection probabilities are listed for reference in Table 2.
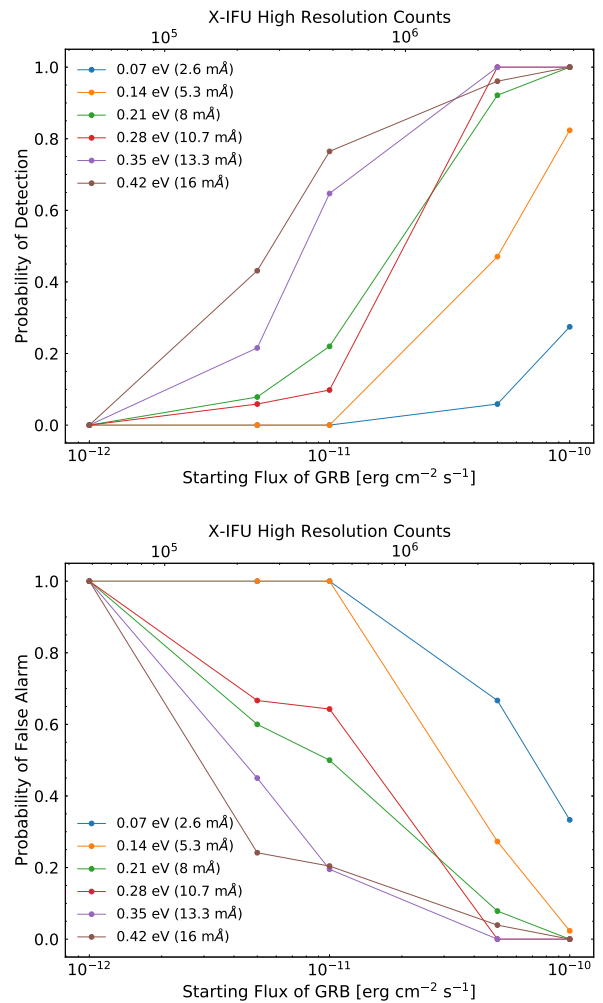

Fig. 2: *Top:* Detection probability by O VII and O VIII absorption features for each EW simulated in the 35 mm defocused configuration of the *Athena* mirror. *Bottom:* False-alarm probability of WHIM detection by O VII and O VIII absorption features for each EW simulated EW in the 35 mm defocused configuration of the *Athena* mirror. EWs listed are those of O VII.

The bottom panel of Fig. 2 shows the probability that a significant detection of two absorption features separated by the same fixed energy difference is made at an energy that does not match the input energy (within $\Delta E = 1.25$ eV). This results in a false-alarm detection of an O VII-O VIII pair. The probability of a false-alarm detection for a given afterglow flux and line equivalent width is calculated by Equation 2. Opposite to the detection probability, the false-alarm probability decreases with increasing afterglow flux and with increasing line equivalent width. For afterglow spectra with starting fluxes of $F = 10^{-12}$ erg cm^{-2} s^{-1} the chance of a misdetection is near 100% for all equivalent widths. Lines with $\mathrm{EW}_{\mathrm{O\,VII}} \geq 0.21$ eV see the false-alarm probability drop to less than 5% when the starting flux of the GRB afterglow is $F = 5 \times 10^{-11}$ erg cm^{-2} s^{-1}, while lines of $\mathrm{EW}_{\mathrm{O\,VII}} = 0.14$ eV reach this level at $F = 10^{-10}$ erg cm^{-2} s^{-1}.

4.2. Recovery of equivalent width

The equivalent width that is fitted to the O VII and O VIII absorption features in the simulated *Athena* spectrum is of particular in-

Table 2: Minimum O VII observed equivalent width that can be detected at 90%, 50%, and 20% detection probabilities for different GRB afterglow starting fluxes during a 50 ks observation.

$F_{start, 0.3-10\,keV}$ [erg cm^{-2} s^{-1}]	$F_{0.3-10\,keV}$ [erg cm^{-2} s^{-1}]	EW$_{90\%}$ [eV]	EW$_{50\%}$ [eV]	EW$_{20\%}$ [eV]
1×10^{-10}	3.3×10^{-11}	0.17	0.10	< 0.07
5×10^{-11}	1.7×10^{-11}	0.20	0.14	0.09
1×10^{-11}	3.3×10^{-12}	> 0.42	0.33	0.23
5×10^{-12}	1.7×10^{-12}	> 0.42	> 0.42	0.34
1×10^{-12}	3.3×10^{-13}	> 0.42	> 0.42	> 0.42

Notes. Column 1: simulated starting flux (erg cm^{-2} s^{-1}) of the GRB afterglow four hours after the outburst began; Column 2: 0.3–10 keV average absorbed flux (erg cm^{-2} s^{-1}) during a 50 ks observation of a GRB afterglow with the X-IFU; Column 3: Minimum observed equivalent width (eV) of O VII with a 90% probability of detection at a minimum significance of 90% by the X-IFU; Column 4: Minimum observed equivalent width (eV) of O VII with a 50% probability of detection at a minimum significance of 90% by the X-IFU; Column 5: Minimum observed equivalent width (eV) of O VII with a 20% probability of detection at a minimum significance of 90% by the X-IFU.

terest because it shows the capability of the X-IFU to reproduce and to measure the characteristics of narrow absorption features. The equivalent width is calculated from the `normalisation` parameter of the `zgauss` component of the fitted spectral model for all O VII-O VIII absorption line pairs that were detected with at least a 90% significance and were detected at the correct redshift during the analysis.

The O VII equivalent width distributions from the fitted simulated spectra for all fluxes are shown in Fig. 3. Each distribution consists of the O VII equivalent width that was fitted during the blind line search for significantly detected absorption features of a given input equivalent width at the correct redshift, z_{WHIM}. The median of the measured equivalent width distribution is marked by a blue-dash line while the input equivalent width is marked by a red-dash line. The 1σ error of the distribution is shaded in blue. The figure shows that for EW$_{O\,VII} \geq 0.14$ eV, the X-IFU can recover the equivalent width of the input lines to within 1σ of the observed equivalent width. However, all distributions in Fig. 3 contain outliers to the 1σ range of the input equivalent width. These outliers arise from real absorption features detected in afterglow spectra with $F_{start} < 5 \times 10^{-11}$ erg cm^{-2} s^{-1}. For line equivalent widths of EW$_{O\,VII} \geq 0.35$ eV, Fig. 2 shows that a fainter GRB afterglow of 10^{-11} erg cm^{-2} s^{-1} will give at least a 70% chance of detecting the absorber in comparison to less than a 20% chance for weaker absorbers. Therefore, the distributions in Fig. 3 with high equivalent widths contain measurements from significant detections of absorption features in fainter afterglow spectra. The low flux of the afterglow results in the equivalent widths of the absorption lines not being measured within the 1σ range of the input equivalent width. Figure 4 shows these equivalent width distributions when detections made from spectra with $F_{start} < 5 \times 10^{-11}$ erg cm^{-2} s^{-1} are excluded. The distributions show fewer outliers outside the 1σ range in comparison to those present in Fig. 3, while the recovered equivalent width lies closer to the input.

The distributions for absorbers of low equivalent widths, in particular EW$_{OVII} = 0.07$ eV, are visually poorer than those of high equivalent widths since there are less significant detections made at low equivalent widths. Figure 2 shows that the probability of detection for EW$_{OVII} = 0.07$ eV remains low for all fluxes, reaching a maximum of approximately 30% for the high-
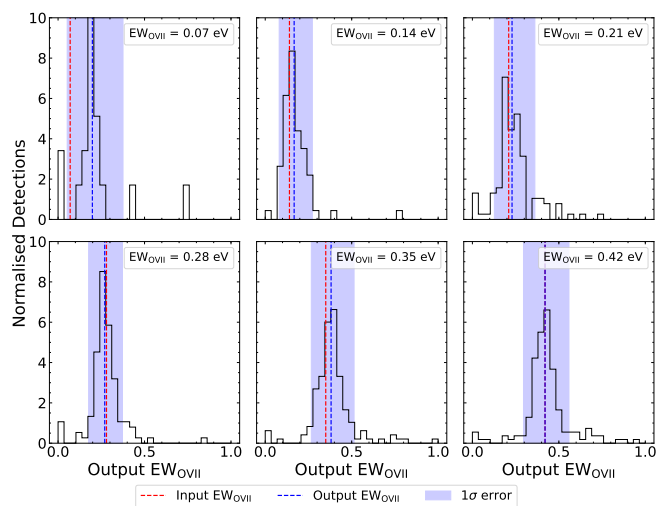

Fig. 3: Distributions of the fitted O VII equivalent widths in eV for each input O VII equivalent width from GRB afterglow spectra with $F_{start} = 10^{-12}$–10^{-10} erg cm^{-2} s^{-1}. The input equivalent width is represented by the red dashed line and the median equivalent width of the distribution is shown by the blue dashed line. The blue shaded area is the 1σ interval of the distribution.

est flux simulated. In comparison, EW$_{OVII} \geq 0.21$ eV reach a near 100% probability of detection for $F_{start} \geq 5 \times 10^{-11}$ erg cm^{-2} s^{-1}. The number of detections in each distribution of Fig. 3 is 17, 66, 111, 109, 140, and 159 for EW$_{OVII} = 0.07$, 0.14, 0.21, 0.28, 0.35, and 0.42 eV, respectively. Therefore, the sample size of each distribution varies due to the ability of the X-IFU to detect significant absorption features of high equivalent widths with a much higher probability.

The distributions of Figs. 3 and 4 exhibit a positive shift between the median of the detected equivalent widths and the input equivalent width from the simulated spectra. Each distribution exhibits broadening about the input equivalent width due to the Eddington bias (Eddington 1913, 1940) and, therefore, contains simulated absorption features of a mean equivalent width, EW with a variance, ΔEW. Since the distributions consist only of O VII features that were detected above a 90% significance level at the correct absorber redshift during the blind-line fitting process, the positive shift between the median and the input equivalent width of each distribution increases with decreasing equivalent width. For higher equivalent widths that are well above the detector threshold, there is an equal probability that the equivalent width of a significant feature will be detected with EW + ΔEW or EW – ΔEW. However, as the detector threshold is approached it becomes more likely that a significant detection is made for EW + ΔEW, thus introducing a positive shift in the observed distributions for lines with low equivalent widths. The EW$_{O\,VII} = 0.07$ eV distribution of both figures samples very few absorbers because of its low input equivalent width, resulting in few significant detections being made during the blind line analysis. It can be concluded that the equivalent width of these absorption features is too small to be accurately measured with the GRB afterglow fluxes simulated in this paper.

4.3. Effect of galactic absorption on the detection of O VII and O VIII

The rest energies of O VII and O VIII (574 eV and 654 eV, respectively) occur near the 200 eV low energy threshold of the X-IFU
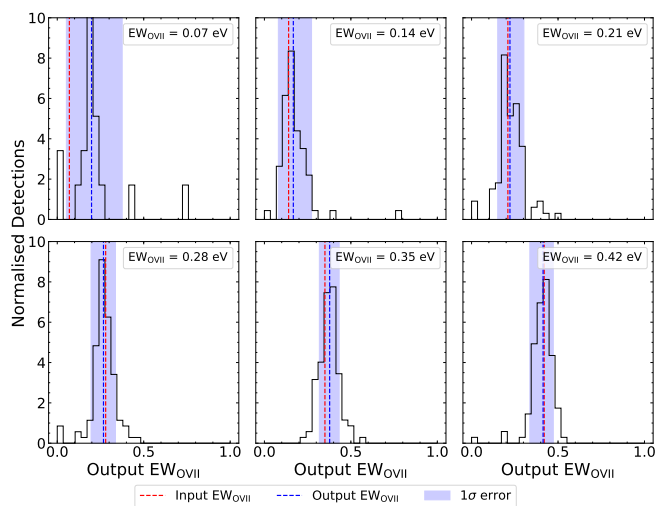
Fig. 4: Distributions of the fitted O VII equivalent widths in eV for each input O VII equivalent width from GRB afterglow spectra with $F \geq 5 \times 10^{-11} \, \mathrm{erg \, cm^{-2} \, s^{-1}}$. The input equivalent width is represented by the red dashed line and the median equivalent width of the distribution is shown by the blue dashed line. The blue shaded area is the 1σ interval of the distribution.

instrument. The energies of their absorption features are redshifted to lower energies by the redshift of the originating absorber. As GRBs occur at an average redshift of 2, it is possible to obtain absorption features from the WHIM in afterglow spectra up to that redshift. However, once a WHIM filament reaches a redshift of $z_{\mathrm{WHIM}} = 1$, an O VII absorption feature will occur at an energy of 287 eV while O VIII will be at 327 eV. While these energies are still within the energy range of the X-IFU, they occur at energies within the afterglow spectrum that are significantly absorbed by the interstellar medium within the Milky Way.

To assess the impact that Galactic absorption along the line of sight has on the detection of O VII and O VIII, SIXTE simulations of a GRB afterglow were executed for varying hydrogen column densities within the Milky Way galaxy and for varying WHIM redshifts, z_{WHIM}. The properties of the GRB afterglow are as in Table 1, while the Galactic absorption parameter of the local galaxy is varied from $10^{20}-10^{22} \, \mathrm{cm^{-2}}$. This range represents the varied distribution of N_{H} columns in the Milky Way, where typical values of $10^{22} \, \mathrm{cm^{-2}}$ originate within the Galactic plane and lower values of $10^{20} \, \mathrm{cm^{-2}}$ occur at regions of high Galactic latitude. The redshift of the absorption features is varied from $z_{\mathrm{WHIM}} = 0$–0.5. The O VII absorption lines have an equivalent width of 0.28 eV while the equivalent width of O VIII is 0.19 eV. The starting flux of the afterglow is set to $5 \times 10^{-11} \, \mathrm{erg \, cm^{-2} \, s^{-1}}$. From the results presented in Sect. 4.1, this combination of equivalent width and starting flux should provide a detection probability of both lines close to unity, based on a Galactic hydrogen column density of $2 \times 10^{20} \, \mathrm{cm^{-2}}$. The spectra are analysed using the blind line fitting technique of Sect. 3.1 and if the line detection is determined significant at at least a 90% threshold and is located at the correct redshift, the true single line significance of each line is calculated using the normalisation parameter, K of the Gaussian absorption component by $K/\Delta K$ (Bonamente 2018). The combined line significance of the O VII-O VIII pair is calculated by adding each single line significance in quadrature. For each combination of hydrogen column density and WHIM redshift, ten spectra are simulated. The combined line significance from all ten spectra are

used to determine the average significance and the 1σ error for each column density and redshift.

Three simulated spectra are shown in Fig. 5. The spectra show a small energy range around the O VII and O VIII absorption features, originating from a WHIM absorber at $z_{\mathrm{WHIM}} = 0.3$. For $N_{\mathrm{H}} = 10^{20} \, \mathrm{cm^{-2}}$, the single line significance of O VII is calculated to be 4.7σ while O VIII has a calculated single line significance of 3.1σ, giving a combined statistical significance of 5.6σ. The O VII absorption feature is detected at slightly higher significance than O VIII because of its higher input equivalent width. For $N_{\mathrm{H}} = 10^{21} \, \mathrm{cm^{-2}}$, the single line significance of O VII and O VIII are 2.6σ and 2.9σ, respectively, giving a combined significance of 3.9σ. The detection significance of the lines has decreased with the increase in the hydrogen column density simulated owing to the excess absorption occurring at the energy of the lines. Inspite of the higher input equivalent width into the simulated spectra of O VII over O VIII, the higher absorption from the local galaxy causes it to be detected at a slightly lower significance than O VIII. For the highest simulated hydrogen column density of $N_{\mathrm{H}} = 10^{22} \, \mathrm{cm^{-2}}$, the X-IFU instrument does not detect any counts below $\approx 0.42 \, \mathrm{keV}$. Neither O VII nor O VIII are detected significantly within the spectrum because of the high level of Galactic absorption. These spectra have in excess of 10^6 high resolution X-IFU counts in the 0.3–10 keV energy range, suggesting that a detection should be made following the results presented in Fig. 2. However, a detection will not be deemed significant in spectra with a high hydrogen column density if the total number of high resolution X-IFU counts in the energy range of the O VII-O VIII pair is too low, as in the bottom panel of Fig. 5. Therefore, a bright afterglow spectrum with a high count rate over the full X-IFU energy range may not detect absorption features at the soft X-ray energy range of the spectrum due to extreme local hydrogen absorption along the line of sight to the GRB.

Figure 6 shows the effect of the Galactic hydrogen column density on the detection significance of an O VII-O VIII absorption pair. As the column density of hydrogen in the local galaxy increases, the combined line significance of O VII-O VIII decreases. Increasing the redshift of the WHIM absorption also results in a reduction in the detection significance. For higher redshifts, the lines occur in the afterglow spectrum at softer energies where the absorption from local hydrogen is more prominent, resulting in a lower line significance. A high local hydrogen column density and a high redshift can result in O VII, or both O VII and O VIII, not being detectable in the spectrum, as seen in the bottom panel of Fig. 5. However, O VIII may still be detected. In this case, the combined line significance is simply the true significance of the O VIII absorption feature.

The number of independent resolution elements N in the blind line search of the spectrum is calculated as in Bonamente (2018) by $N = E_{\mathrm{O \, VII}} \cdot \Delta z_{\mathrm{WHIM}}/\sigma_E$, where $\mathrm{E_{O \, VII}}$ is the rest energy of O VII, Δz_{WHIM} is the redshift range in which absorption features are searched for, and σ_E is the energy spectral resolution of the X-IFU. The X-IFU spectral resolution of $\sigma_E = 2.5 \, \mathrm{eV}$ and the WHIM redshift range of $\Delta z_{\mathrm{WHIM}} = 0.5$ gives 115 independent opportunities to detect a feature during the search. For each absorption feature to have a true line significance of at least 3σ, a minimum combined line significance of 4.2σ is required. Figure 6 shows that to obtain a detection with a combined line significance of 4.2σ or greater, the hydrogen column density of the local galaxy must be less than $\sim 10^{21} \, \mathrm{cm^{-2}}$. From Bonamente (2018) the probability of detecting two random fluctuations both of 3σ in a blind line search having 100 independent trials is 3.67%, meaning it could be concluded that the detected fluctu-
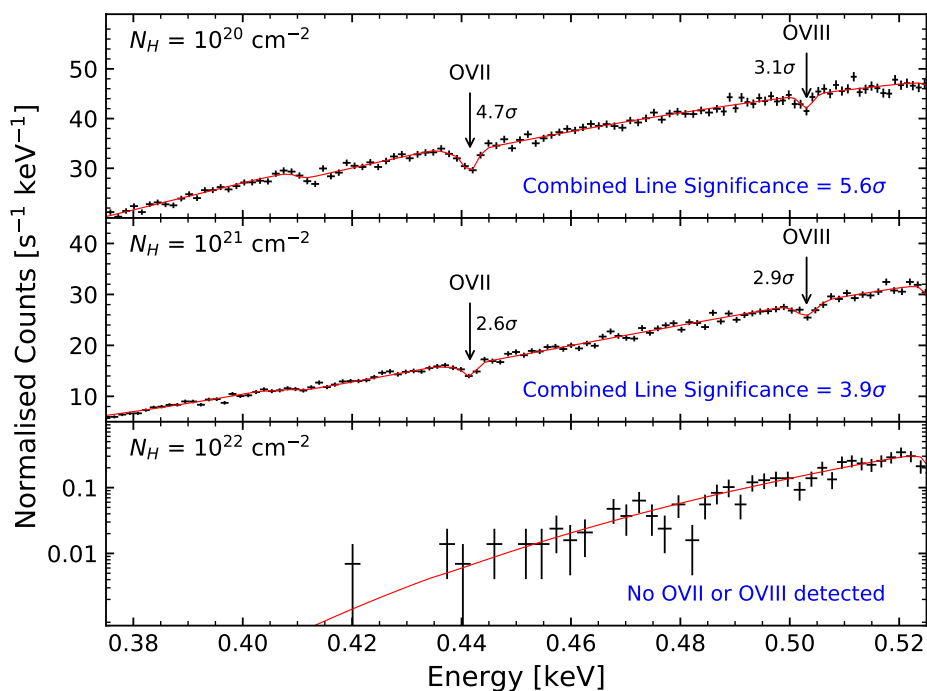
Fig. 5: Simulated X-IFU spectrum for varying Milky Way hydrogen column densities with O VII and O VIII absorption features at $z_{WHIM} = 0.3$. Input lines have equivalent widths of $EW_{O\,VII} = 0.28$ eV and $EW_{O\,VIII} = 0.19$ eV. Afterglow spectra have a starting flux of $F_{start} = 5 \times 10^{-11}$ erg cm^{-2} s^{-1}. *Top:* Hydrogen column density of 10^{20} cm^{-2}. *Middle:* Hydrogen column density of 10^{21} cm^{-2}. *Bottom:* Hydrogen column density of 10^{22} cm^{-2}.
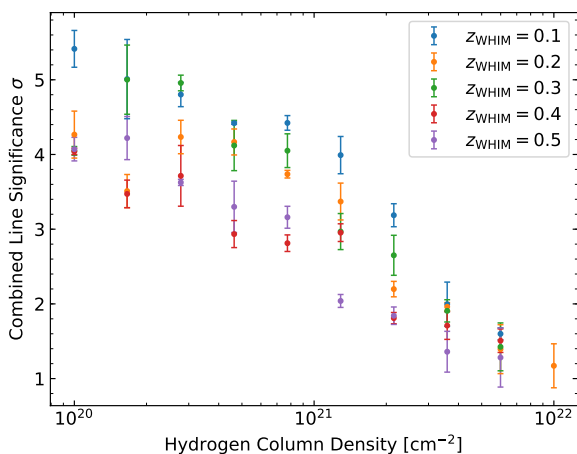

Fig. 6: Combined line significance of an O VII-O VIII pair detection for different WHIM absorber redshifts as a function of the hydrogen column density in the Milky Way galaxy for an afterglow flux of $F_{start} = 5 \times 10^{-11}$ erg cm^{-2} s^{-1} and O VII line equivalent width of $EW_{O\,VII} = 0.28$ eV. Error bars represent the 1σ scatter among the 10 simulated spectra.

ations are random. However, if both fluctuations are detected at 3.2σ in a blind line search having the same number of trials, the probability that the fluctuations are random is reduced to 0.4%, meaning there is a much greater chance that these fluctuations

are real. Two 3.2σ detections result in a combined line significance of 4.5σ. At this significance, Fig. 6 shows that the hydrogen column density must be less than 8×10^{20} cm^{-2}.

5. Discussion

If GRBs are used to detect the WHIM with a minimum limit of 75% confidence of detection, *Athena* will need to target GRB afterglows of $F_{start} > 5 \times 10^{-11}$ erg cm^{-2} s^{-1} to detect an O VII-O VIII pair of minimum equivalent width 0.18 eV and 0.12 eV, respectively. This flux provides a false-alarm probability of less than 10% for detecting the WHIM with lines of this equivalent width. Strong O VII absorbers of 0.39–0.42 eV can be detected with a probability of 75% at 10^{-11} erg cm^{-2} s^{-1} and a false-alarm probability of 20%. Brighter afterglows of $F_{start} \sim 10^{-10}$ erg cm^{-2} s^{-1} will be required to detect O VII and O VIII absorption features of 0.13 eV and of 0.08 eV equivalent width, respectively. These starting flux thresholds, and corresponding X-IFU count rates and 0.3–10 keV average absorbed fluxes, are listed in the first, second, and third Columns of Table 3, while the minimum detectable equivalent widths of the O VII-O VIII pair are listed in Columns 5 and 7.

To determine how many GRB afterglows occur per year in line with the flux thresholds of Table 3 and, therefore, allow the detection of the WHIM with *Athena*, the *Swift*-XRT population of GRB afterglows is considered (Evans et al. 2007, 2009). From the *Swift* population all long GRBs are considered, with a limit of $T_{90} > 4$ s to exclude any short GRBs with extended emission, producing a sample of 948 GRB afterglows. The light curves of the afterglows are interpolated and are assessed to determine
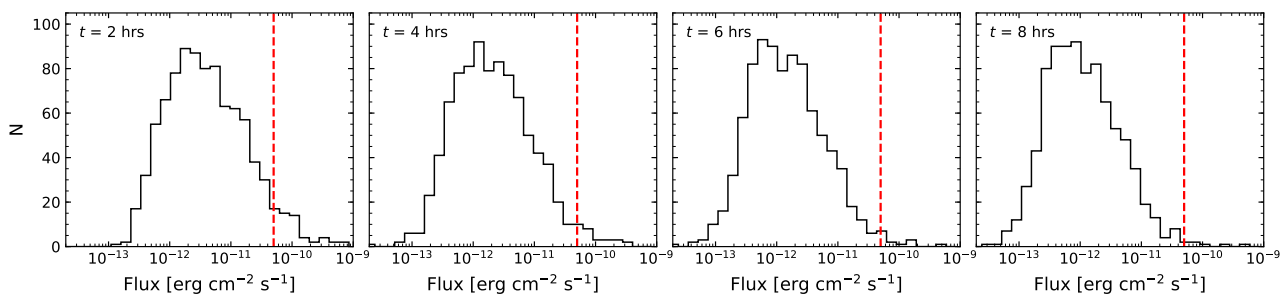
Fig. 7: Flux distribution of GRBs observed by *Swift*-XRT with $T_{90} > 4\,\mathrm{s}$ (long bursts only) at two hours (left), four hours (middle left), six hours (middle right), and eight hours (right) after the initial outburst began. The red dashed line indicates a flux of $5 \times 10^{-11}\,\mathrm{erg\,cm^{-2}\,s^{-1}}$.

a flux value at a given observation time. If no interpolated flux value is present for the observation time, it is excluded from the sample. Figure 7 shows the flux distributions of 903, 892, 889, and 889 GRB afterglows at two, four, six, and eight hours, respectively, after the initial outburst began.

The original ToO requirement for *Athena* aimed to observe 67% of GRB afterglows in a 60% field of regard within four hours for 50 ks. However, to account for the decaying nature of GRB afterglow fluence with time the requirement has been reformulated. The science requirement now aims to observe GRB afterglows that can provide spectra with at least one million counts (Jaubert & Debout 2019). The reformulation allows the X-IFU to target dimmer afterglows early in their afterglow phase or target brighter afterglows at later times, provided that the minimum number of spectral counts are obtained. This can be achieved by optimizing the cooling chain scheme of the X-IFU with a partial heat-up (PHU) operational strategy, whereby the regeneration of the cooling chain between X-IFU observations is split into two sub-phases. The first heat-up (HU) phase begins immediately after an X-IFU observation and occurs for a duration that provides the detector with sufficient cold time to perform a potential ToO observation that would meet the required count rate. Therefore, depending on the magnitude of repointing required, the brightness of the afterglow, and the operational phase of the X-IFU cooling chain, the reaction time of *Athena* will vary. For an *Athena* ToO reaction time of four hours, the four hour distribution of Fig. 7 shows that the population of GRBs higher than the threshold starting fluxes of 1, 5, and $10 \times 10^{-11}\,\mathrm{erg\,cm^{-2}\,s^{-1}}$ are 15%, 3%, and 1% of the total. These fluxes allow for the detection of absorption features with $\mathrm{EW_{O\,VII}} \geq 0.39$, 0.18, and 0.13 eV, respectively. To detect lines of $\mathrm{EW_{O\,VII}} < 0.13\,\mathrm{eV}$, a brighter afterglow would be required. However, less than 1% of the total population of GRB afterglows detected by *Swift* have a flux of $F > 10^{-10}\,\mathrm{erg\,cm^{-2}\,s^{-1}}$ four hours after the initial outburst, and so, it is unlikely that such a burst would contribute to the detection of the WHIM. Alternatively, a brighter afterglow could be seen if the X-IFU observation begins sooner than four hours after trigger. If *Athena* can react to a GRB trigger and repoint at the afterglow within two hours, the population of afterglows with starting fluxes greater than $10^{-10}\,\mathrm{erg\,cm^{-2}\,s^{-1}}$ increases to 3%. This allows for a more likely detection of weaker absorption systems with $\mathrm{EW_{O\,VII}} < 0.13\,\mathrm{eV}$. A longer reaction time of eight hours would result in the GRB afterglow population decreasing to 6%, 1%, and 0.5% for starting fluxes of 1, 5, and $10 \times 10^{-11}\,\mathrm{erg\,cm^{-2}\,s^{-1}}$, meaning that a significant detection of the WHIM becomes unlikely, but not impossible.

The exact number of GRBs that *Athena* will detect per year will depend on how the bursts are triggered. Currently, γ-ray observatories such as the Neils Gehrels Swift Observatory (Gehrels et al. 2004), *Fermi*-GBM (Meegan et al. 2009), and INTEGRAL (Winkler et al. 2003) trigger on and perform follow-up observations of GRBs. They provide redshift and localisation information to X-ray observatories to facilitate further X-ray afterglow follow up. However, these missions have all exceeded their nominal mission lifetime. Future missions with triggering capabilities planned to be operating during the lifetime of *Athena* include the Space Variable Objects Monitor (SVOM; Cordier et al. 2015) and the Wide Field Monitor (Hernanz et al. 2018) on board the Enhanced X-ray Timing and Polarization mission (eXTP; Zhang et al. 2016). A number of proposed missions are currently at concept level, such as the Transient High Energy Sky and Early Universe Surveyor (THESEUS; Amati et al. 2018) and the All-Sky Medium Energy Gamma-ray Observatory (AMEGO; McEnery et al. 2019), both capable of triggering and localising GRBs. In addition, constellations of low-cost CubeSat missions capable of detecting gamma-rays, such as BurstCube (Racusin et al. 2017) and HERMES (Fuschino et al. 2019), could provide trigger and localisation information. A mission with such capabilities is required to increase the rate of GRB detections per year with accurate localisations and redshifts, so that rapid repointing of the *Athena* X-IFU can be achieved to conduct high resolution X-ray spectroscopy of the WHIM.

Table 3 presents the detection parameters for O VII-O VIII absorption features against GRB afterglows of varying starting fluxes. Column 5 of Table 3 reports the minimum observed equivalent width required to detect an O VII absorption feature of an O VII-O VIII pair for each afterglow flux in Column 1, with the O VIII minimum equivalent width of that same pair in Column 9. Columns 6, 7, and 8 report the number of O VII absorption systems per unit redshift above the given X-IFU observed equivalent width threshold for distributions of the WHIM at $z = 0.1$, 0.2, and 0.5, respectively. Similarly, Columns 10, 11, and 12 report the number of O VIII absorption systems per unit redshift above the observed equivalent width threshold in Column 9. These are calculated from the EAGLE cosmological hydrodynamical simulations (Schaye et al. 2015; Crain et al. 2015; McAlpine et al. 2016), using the methods described in Wijers et al. (2019). The number of O VII and O VIII absorbers decreases with increasing redshift. This is a result of the rest frame equivalent width increasing with increasing redshift, for a fixed observed equivalent width measured in energy. The number of absorbers at $z = 0.1$ and at $z = 0.2$ show little evolution, while the decrease in absorbers becomes prominent at $z = 0.5$.

Table 3: Detection parameters of the WHIM for the X-IFU.

F_{start} [erg cm^{-2} s^{-1}]	$F_{0.3-10}$ [erg cm^{-2} s^{-1}]	X-IFU Counts (in 50 ks)	# GRBs %	EW$_{O\,VII}$ [eV]	$dN(>EW_{O\,VII})/dz$			EW$_{O\,VIII}$ [eV]	$dN(>EW_{O\,VIII})/dz$		
					$z=0.1$	$z=0.2$	$z=0.5$		$z=0.1$	$z=0.2$	$z=0.5$
1×10^{-10}	3.3×10^{-11}	4.8×10^{6}	1.46	0.13	2.39	2.40	1.81	0.09	2.32	2.41	2.44
5×10^{-11}	1.7×10^{-11}	2.4×10^{6}	2.8	0.18	1.33	1.32	0.85	0.12	1.46	1.50	1.46
4×10^{-11}	1.4×10^{-11}	1.9×10^{6}	3.81	0.20	1.04	1.03	0.63	0.13	1.25	1.29	1.24
3×10^{-11}	1.0×10^{-11}	1.4×10^{6}	4.59	0.30	0.30	0.31	0.14	0.20	0.48	0.47	0.37
1×10^{-11}	3.3×10^{-12}	4.8×10^{5}	15.58	0.39	0.11	0.13	0.04	0.26	0.20	0.18	0.12

Notes. Column 1: simulated starting flux (erg cm^{-2} s^{-1}) of the GRB afterglow; Column 2: 0.3–10 keV average absorbed flux (erg cm^{-2} s^{-1}) during a 50 ks observation of a GRB afterglow with the X-IFU; Column 3: High resolution counts collected during the 50 ks observation of the GRB afterglow; Column 4: the percentage of GRB afterglows per year above the flux in Column 2 based on the Swift population of GRBs; Column 5: Minimum equivalent width (eV) of O VII for a 75% chance of detection with the X-IFU; Column 6–8: Expected number of absorption systems per unit redshift for O VII above EW in Column 5 at redshifts $z = 0.1$, 0.2 and 0.5; Column 9: Minimum equivalent width (eV) of O VIII for a 75% chance of detection with the X-IFU; Column 10–12: Expected number of absorption systems per unit redshift for O VIII above EW in Column 9 at redshifts $z = 0.1$, 0.2 and 0.5.
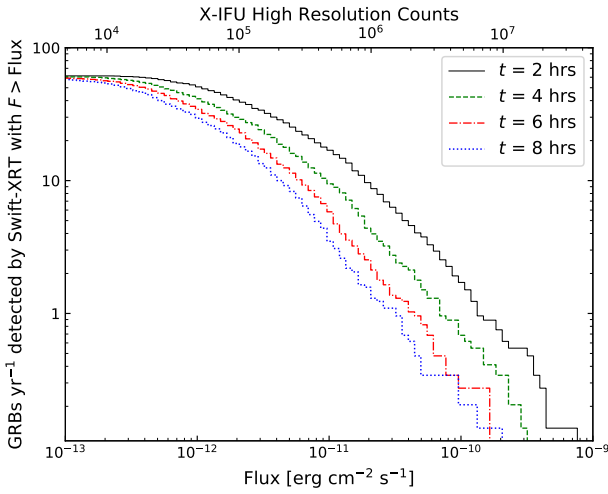

Fig. 8: Cumulative number of GRBs afterglows detected per year by *Swift*-XRT with $T_{90} > 4$ s (long bursts only) as a function of flux and X-IFU counts for observations made at two, four, six, and eight hours after the initial outburst began.

Figure 9 shows the cumulative annual absorber detection rate of *Athena*, based on the predicted GRB population and the reformulated ToO requirement. The distribution is described by the function,

$$N = \frac{dN(>EW)}{dz} \cdot dz \cdot N_{Athena\,GRBs/yr} \cdot FoR \cdot N_H, \quad (3)$$

where $dN(>EW)/dz$ is the number of absorbers per unit redshift above a minimum observed equivalent width given in Table 3, dz is the absorption length for the WHIM, $N_{Athena\,GRBs/yr}$ is the predicted number of GRB afterglows that will be observed by *Athena* per year to detect the WHIM, $FoR = 0.6$ is the field of regard of *Athena*, and N_H is the fraction of the field of regard with a suitable Galactic hydrogen column to observe the absorption features. Given that the average redshift of a GRB is $z_{GRB} \approx 2$, it is assumed that the absorption length for the WHIM in a GRB observation will be $\Delta z_{WHIM} = 1$, as higher redshift absorption features are outside the X-IFU energy range.

Two distributions of the detected absorber rate are shown in Fig. 9, highlighting the difference between the detection rates when probing different redshifts of the WHIM. At

EW ≈ 0.35–0.39 eV, the rate of GRB detection for afterglows with $F > 10^{-11}$ erg cm^{-2} s^{-1} is approximately 15% of the total population for a reaction time of four hours and approximately 30% for a reaction time of two hours. This results in the distribution of detected absorbers per year increasing slightly, even with a significant decrease in the number of absorbers per unit redshift. Between EW ≈ 0.25–0.35 eV the cumulative number of detected absorbers levels off, although there is an increasing number of absorbers with smaller equivalent widths, as the rate of GRB afterglows decreases with increasing flux. The distributions show a significant increase in the number of absorbers detected per year between observed equivalent widths of 0.13–0.25 eV. This is a result of the high number of absorbers expected to have minimum equivalent widths in this range, in spite of the low population of high flux GRBs.

The predicted annual rate of GRB detection with THESEUS is 300–700 GRBs yr^{-1} (Amati et al. 2018), a relative increase by a factor of ≈ 5–10 on the annual rate currently detected by *Swift*. Figure 8 shows the *Swift*-XRT cumulative distribution of GRB afterglows as a function of the observation starting flux for observations beginning two, four, six, and eight hours after the outburst was triggered. Assuming that *Athena* can follow up on all GRBs within its field of regard triggered by a spacecraft such as THESEUS, the *Swift*-XRT sample of afterglow observations can be used to provide an estimate for the number of afterglows that *Athena* will observe. This is calculated by $N_{Athena\,GRBs/yr} = N_{THESEUS\,GRBs/yr} \times N_{Swift\,GRBs/yr}$, where $N_{Swift\,GRBs/yr}$ is derived from Fig. 8 by weighting each reaction time distribution in accordance with simulated *Athena* ToO response times (Jaubert & Debout 2019) and $N_{THESEUS\,GRBs/yr}$ is the relative number of GRB detections of THESEUS compared to *Swift*. This provides an upper and lower limit to the number of GRBs, and therefore, absorbers per year that *Athena* may observe. Figure 9 shows that the lower predicted GRB detection rate amounts to approximately 17 absorbers per year, while the higher predicted rate gives 34 absorbers per year detected with *Athena* through O VII-O VIII absorption pairs. If $z = 0.5$ contributes most to the survey path, the number of absorbers detected decreases to 11–22 per year. This is a relative increase of 20–25% on the absorbers detected per year in comparison to the previous ToO requirement to observe GRB afterglows for 50 ks within four hours of the initial trigger.

Wijers et al. (2019) presented the relationship between the equivalent width and column density of O VII and O VIII absorption systems. A linear relation is present between the absorber
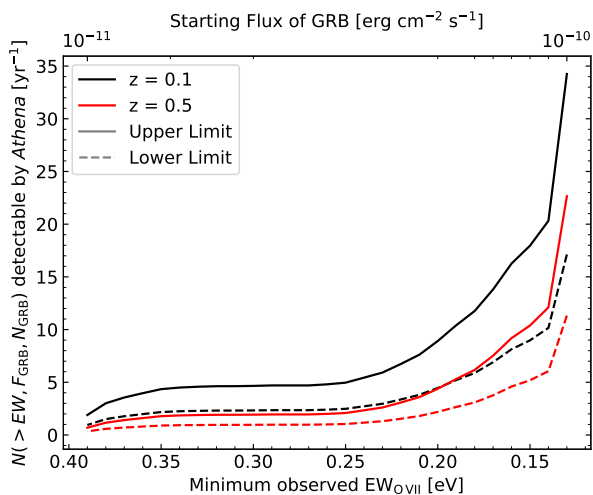
Fig. 9: Cumulative number of O VII-O VIII absorbers detectable by *Athena* per year above a minimum observed equivalent width for distributions of the WHIM at $z = 0.1$ (black) and $z = 0.5$ (red) as a function of the starting flux of the GRB afterglow and the predicted number of afterglows above that flux.

equivalent width and column density for all but the highest column densities and equivalent widths, where the relationship becomes non-linear. Wijers et al. (2019) show that a high column density traces high-density gas, typically associated with the circumgalactic medium (CGM). The relationship between the column density and the equivalent width of absorbers is highly scattered and the distinction of these parameters between the CGM and IGM is not well defined. Therefore, the number of absorbers quoted contain absorbers of the CGM together with filaments of the WHIM. In addition, the work presented here simulates only O VII-O VIII absorption pairs of a fixed ratio. Spectra originating from WHIM absorbers may contain features from other ions, depending on the temperature and density of the gas, such as Ne IX, Ne X, Fe XVII, Fe XVIII, etc. Searching for these ions in afterglow spectra will aid the detection probability of absorbers, and so, the number of absorbers detectable by *Athena* quoted in this paper is of a lower limit.

The results discussed above refer to the number of absorption systems of a given equivalent width from afterglow spectra simulated with a local hydrogen column density of 2×10^{20} cm^{-2} and a hydrogen column density intrinsic to the GRB of 10^{22} cm^{-2}. Willingale et al. (2013) show that the N_H density distribution of GRB afterglows observed by *Swift*-XRT peaks at 2×10^{21} cm^{-2}, a factor of ten greater than the spectra simulated in this work to calculate the detection probability of the WHIM. Section 4.3 presented the impact of a higher hydrogen column density within the Milky Way on the detection of absorption features imprinted on an afterglow spectrum. Figure 6 showed that to detect an O VII-O VIII absorption pair originating from the same WHIM filament with a combined line significance greater than 4.5σ, the N_H column cannot exceed 8×10^{20} cm^{-2}. Various surveys have been performed to determine the hydrogen distribution in the Milky Way (e.g. Dickey & Lockman 1990; Kalberla et al. 2005; HI4PI Collaboration et al. 2016). HI4PI Collaboration et al. (2016) show that approximately 35% of lines of sight have column densities of $N_H > 8 \times 10^{20}$ cm^{-2} and are located between an average of 22° North and 24° South of the galactic plane. Because of the effect that such levels of absorption have on the detection of WHIM features, these regions of the sky should be

excluded when searching for WHIM absorption features in GRB afterglow spectra. This results in a 25% reduction of the number of absorption systems that can be detected by *Athena* within the field of regard, which is included in Fig 9. Therefore, regions of high Galactic latitude are favoured to observe WHIM absorption features, which are known to have large uncertainties on the level of Galactic absorption (e.g. Dickey & Lockman 1990), and differences between the adopted survey (e.g. Kalberla et al. 2005 and HI4PI Collaboration et al. 2016). However, due to the low levels of Galactic absorption at high latitudes, $\approx 1.8 \times 10^{20}$ cm^{-2} for $|b| > 60°$, it is not foreseen that these large uncertainties will significantly affect the ability to detect absorption features of the WHIM.

The combined line significance required to claim a real detection with high certainty depends on the number of independent spectral elements within the blind line search. A 4.5σ combined detection for 100 independent redshift trials of a blind line search, as in this survey, results in a probability of 0.4% that the fluctuations could be random. However, a 4.5σ combined significance, or 3.2σ each, for 40 spectral elements searched in the spectrum results in a 0.08% chance of the fluctuations being random. A reduced blind line search region could be achieved with a low redshift GRB as the background source or with an a priori redshift from UV data or known galaxy locations, as in Kovács et al. (2019) and Ahoranta et al. (2020).

This work assumes a high intrinsic hydrogen column density of 10^{22} cm^{-2} for the host galaxy of the GRB. The exact origin of this intrinsic absorption in afterglow spectra has been studied (e.g. Schady et al. 2011; Watson et al. 2013). Evans et al. (2009) present the distribution of intrinsic column density of GRB afterglows observed by *Swift*-XRT, peaking at approximately 10^{21} cm^{-2}, when GRBs of unknown redshift are located at $z_{GRB} = 0$, and peaking at 10^{22} cm^{-2}, when $z_{GRB} = 2.23$ for those with no recorded redshift value. A mean value of $\approx 5 \times 10^{21}$ cm^{-2} was found by Campana et al. (2012) when using only afterglows of known redshift in the sample. This absorption from the host galaxy of the afterglow will have a similar impact to that of the Milky Way, meaning a lower intrinsic column will increase the significance of these line detections. Using the *Swift*-XRT population of observed GRB afterglows of known redshift, a relationship has been seen between the intrinsic column density of the host galaxy and the redshift of the GRB where a lower redshift is associated with a lower intrinsic hydrogen column density (Campana et al. 2012). However, it has also been suggested that this observation may be due to a bias in dust extinction (Watson & Jakobsson 2012). If this relationship holds, then targeting lower redshift GRB afterglows will result in a lower intrinsic hydrogen column density. This can be combined with observing afterglows along lines of sight with a low hydrogen column density in the Milky Way to increase the chance of a significant detection of the WHIM.

6. Conclusions

This work has assessed the capability of the *Athena* X-IFU to detect the missing baryons of the WHIM, through O VII and O VIII absorption features at rest-frame energies of 574 eV and 654 eV, respectively, in the X-ray afterglow spectra of GRBs. The results of this study are summarised as follows.

1. To obtain a 75% detection probability of O VII and O VIII with a minimum observed equivalent width of EW$_{O VII}$= 0.13–0.39 eV and EW$_{O VIII}$= 0.09–0.26 eV, *Athena* should target GRB afterglows of $F_{start} \geq 2 \times 10^{-11}$ erg cm^{-2} s^{-1}, or $\gtrsim 10^6$

high resolution X-IFU counts, in the 0.3–10 keV energy band. This results in 15–30 GRBs yr^{-1} within *Athena*'s field of regard, allowing for the detection of 11–34 absorbers per year through O VII-O VIII pairs with the X-IFU.

2. Absorption systems weaker than 0.13 eV will require GRB afterglows of $F_{\text{start}} > 10^{-10}$ erg cm^{-2} s^{-1}, or $\gtrsim 5 \times 10^6$ high resolution X-IFU counts, to obtain a 75% chance of detection. This amounts to less than 1% of the GRB population if the observation begins four hours after the GRB trigger. A shorter ToO reaction time, or longer observation, would be required to observe an afterglow with an observed starting flux greater than 10^{-10} erg cm^{-2} s^{-1}, to reveal absorption systems with observed EW$_{\text{O VII}} < 0.13$ eV.

3. The X-IFU is capable of measuring the observed equivalent width of narrow absorption features within a 1σ limit for features with EW ≥ 0.14 eV imprinted on afterglow spectra with $F_{\text{start}} \geq 5 \times 10^{-11}$ erg cm^{-2} s^{-1}.

4. The absorption from hydrogen in the local Galaxy and the redshift of WHIM absorbers impacts the significance at which absorption features are detected in the X-IFU spectra. The significance of lines decreases with increasing hydrogen column density and with increasing redshift of the WHIM. To obtain a combined line significance of 4.5σ of an O VII-O VIII absorption pair, a hydrogen column density of $N_{\text{H}} \leq 8 \times 10^{20}$ cm^{-2} along the line of sight is required. This excludes observations of 35% of the sky, located between an average of 22° North and 24° South of the Galactic plane.

The results show that *Athena* will be able to detect the WHIM through O VII-O VIII absorption features using GRB X-ray afterglows as the background source. This study provides limits to the brightness and location of the GRB afterglows that can be observed to reveal the missing baryons of the WHIM with high significance. Depending on the triggering mechanism, the detection rate of GRBs, and the distribution of the WHIM, the work presented shows that *Athena* may detect ≈ 45–137 absorbers through O VII-O VIII absorption pairs with EW$_{\text{O VII}} \geq 0.13$ eV in GRB afterglows throughout the four-year mission.

References

Ackermann, M., Ajello, M., Allafort, A., et al. 2011, ApJ, 743, 171

Ahoranta, J., Nevalainen, J., Wijers, N., et al. 2020, A&A, 634, A106

Amati, L., O'Brien, P., Götz, D., et al. 2018, Advances in Space Research, 62, 191

Arnaud, K. 1996, Astronomical Data Analysis Software and Systems V, Astronomical Society of the Pacific Conference Series, 101, 17

Astropy Collaboration, Price-Whelan, A. M., Sipőcz, B. M., et al. 2018, AJ, 156, 123

Astropy Collaboration, Robitaille, T. P., Tollerud, E. J., et al. 2013, A&A, 558, A33

Barret, D., Lam Trong, T., den Herder, J.-W., et al. 2018, in Society of Photo-Optical Instrumentation Engineers (SPIE) Conference Series, Vol. 10699, Space Telescopes and Instrumentation 2018: Ultraviolet to Gamma Ray, 106991G

Bhat, N. P., Meegan, C. A., von Kienlin, A., et al. 2016, ApJS, 223, 28

Blinnikov, S. I., Novikov, I. D., Perevodchikova, T. V., & Polnarev, A. G. 1984, Soviet Astronomy Letters, 10, 177

Bonamente, M. 2018, arXiv e-prints, arXiv:1810.02207

Bonamente, M., Nevalainen, J., Tilton, E., et al. 2016, MNRAS, 457, 4236

Branchini, E., Ursino, E., Corsi, A., et al. 2009, ApJ, 697, 328

Brand, T. 2016, PhD thesis, Friedrick-Alexander-Universität Erlangen-Nürnberg

Brand, T., Wilms, J., Dauser, T., et al. 2016, in Society of Photo-Optical Instrumentation Engineers (SPIE) Conference Series, Vol. 9905, Space Telescopes and Instrumentation 2018: Ultraviolet to Gamma Ray, 99055F

Burles, S. & Tytler, D. 1998, ApJ, 499, 699

Campana, S., Salvaterra, R., Melandri, A., et al. 2012, MNRAS, 421, 1697

Cash, W. 1979, ApJ, 228, 939

Cen, R. & Ostriker, J. P. 1999, ApJ, 514, 1

Cen, R. & Ostriker, J. P. 2006, ApJ, 650, 560

Cordier, B., Wei, J., Atteia, J. L., et al. 2015, arXiv e-prints, arXiv:1512.03323

Crain, R. A., Schaye, J., Bower, R. G., et al. 2015, MNRAS, 450, 1937

Cucchiara, A., Levan, A. J., Fox, D. B., et al. 2011, ApJ, 736, 7

Cyburt, R. H., Fields, B. D., Olive, K. A., & Yeh, T.-H. 2016, Rev. Mod. Phys., 88, 015004

Dauser, T., Falkner, S., Lorenz, M., et al. 2019, A&A, 630, A66

Davé, R., Cen, R., Ostriker, P., et al. 2001, ApJ, 552, 473

Dickey, J. M. & Lockman, F. J. 1990, ARA&A, 28, 215

Eddington, A. S. 1913, MNRAS, 73, 359

Eddington, A. S., S. 1940, MNRAS, 100, 354

Evans, P. A., Beardmore, A. P., Page, K. L., et al. 2009, MNRAS, 397, 1177

Evans, P. A., Beardmore, A. P., Page, K. L., et al. 2007, A&A, 469, 379

Fiore, F., Nicastro, F., Savaglio, S., Stella, L., & Vietri, M. 2000, ApJ, 544, L7

Fukugita, M., Hogan, C. J., & Peebles, P. J. E. 1998, ApJ, 503, 518

Fuschino, F., Campana, R., Labanti, C., et al. 2019, NIMPRA, 936, 199

Gehrels, N., Chincarini, G., Giommi, P., et al. 2004, ApJ, 611, 1005

Hellsten, U., Gnedin, N. Y., & Miralda-Escudé, J. 1998, ApJ, 509, 56

Hernanz, M., Brandt, S., Feroci, M., et al. 2018, in Society of Photo-Optical Instrumentation Engineers (SPIE) Conference Series, Vol. 10699, Proc. SPIE, 1069948

HI4PI Collaboration, Ben Bekhti, N., Flöer, L., et al. 2016, A&A, 594, A116

Jansen, F., Lumb, D., Altieri, B., et al. 2001, A&A, 365, L1

Jaubert, J. & Debout, V. 2019, in 11th International Workshop on Planning and Scheduling for Space Conference Proceedings, IWPSS 2019, Berkeley

Johnson, S. D., Mulchaey, J. S., Chen, H.-W., et al. 2019, ApJ, 884, L31

Kaastra, J., Finoguenov, A., Nicastro, F., et al. 2013, ArXiv e-prints [arXiv:1306.2324]

Kaastra, J. S. 2017, A&A, 605, A51

Kaastra, J. S. & Bleeker, J. A. M. 2016, A&A, 587, A151

Kaastra, J. S., Werner, N., Herder, J. W. A. d., et al. 2006, ApJ, 652, 189

Kalberla, P. M. W., Burton, W. B., Hartmann, D., et al. 2005, A&A, 440, 775

Kouveliotou, C., Meegan, C. A., Fishman, G. J., et al. 1993, ApJ, 413, L101

Kovács, O. E., Bogdán, Á., Smith, R. K., Kraft, R. P., & Forman, W. R. 2019, ApJ, 872, 83

MacFadyen, A. I. & Woosley, S. E. 1999, ApJ, 524, 262

Margutti, R., Zaninoni, E., Bernardini, M. G., et al. 2013, MNRAS, 428, 729

McAlpine, S., Helly, J. C., Schaller, M., et al. 2016, Astronomy and Computing, 15, 72

McEnery, J., Abel Barrio, J., Agudo, I., et al. 2019, arXiv e-prints, arXiv:1907.07558

Meegan, C., Lichti, G., Bhat, P. N., et al. 2009, ApJ, 702, 791

Meidinger, N., Barbera, M., Emberger, V., et al. 2017, in Society of Photo-Optical Instrumentation Engineers (SPIE) Conference Series, Vol. 10397, Society of Photo-Optical Instrumentation Engineers (SPIE) Conference Series, 103970V

Nicastro, F. 2018, arXiv e-prints, arXiv:1811.03498

Nicastro, F., Kaastra, J., Krongold, Y., et al. 2018, Nature, 558, 406

Nicastro, F., Krongold, Y., Fields, D., et al. 2010, ApJ, 715, 854

Nicastro, F., Mathur, S., Elvis, M., et al. 2005, ApJ, 629, 700

Nicastro, F., Senatore, F., Gupta, A., et al. 2016, MNRAS, 458, L123

Norris, J. P., Cline, T. L., Desai, U. D., & Teegarden, B. J. 1984, Nature, 308, 434

Nousek, J. A., Kouveliotou, C., Grupe, D., et al. 2006, ApJ, 642, 389

O'Brien, P. T., Willingale, R., Osborne, J., et al. 2006, ApJ, 647, 1213

Paczynski, B. 1986, ApJ, 308, L43

Padovani, P., Alexander, D. M., Assef, R. J., et al. 2017, A&ARv, 25, 2

Perna, R. & Loeb, A. 1998, ApJ, 503, L135

Planck Collaboration, Ade, P. A. R., Aghanim, N., et al. 2014, A&A, 571, A1

Protassov, R., van Dyk, D. A., Connors, A., Kashyap, V. L., & Siemiginowska, A. 2002, ApJ, 571, 545

---

[4] http://www.astropy.org

Racusin, J., Perkins, J. S., Briggs, M. S., et al. 2017, arXiv e-prints, arXiv:1708.09292

Rasmussen, A. P., Kahn, S. M., Paerels, F., et al. 2007, ApJ, 656, 129

Schady, P., Savaglio, S., Krühler, T., Greiner, J., & Rau, A. 2011, A&A, 525, A113

Schaye, J., Crain, R. A., Bower, R. G., et al. 2015, MNRAS, 446, 521

Schmid, C., Smith, R., & Wilms, J. 2013, SIMPUT: A File Format for SIMulation inPUT, Tech. rep., Cambridge: HEASARC

Shull, J. M., Smith, B. D., & Danforth, C. W. 2012, ApJ, 759, 23

Spergel, D. N., Verde, L., Peiris, H. V., et al. 2003, ApJS, 148, 175

Tepper-García, T., Richter, P., Schaye, J., et al. 2012, MNRAS, 425, 1640

Verner, D. A., Ferland, G. J., Korista, K. T., & Yakovlev, D. G. 1996, ApJ, 465, 487

Watson, D. & Jakobsson, P. 2012, ApJ, 754, 89

Watson, D., Zafar, T., Andersen, A. C., et al. 2013, ApJ, 768, 23

Weisskopf, M. C., Brinkman, B., Canizares, C., et al. 2002, PASP, 114, 1

Wijers, N. A., Schaye, J., Oppenheimer, B. D., Crain, R. A., & Nicastro, F. 2019, MNRAS, 488, 2947

Williams, R. J., Mathur, S., Nicastro, F., & Elvis, M. 2006, ApJ, 642, L95

Willingale, R. & Mészáros, P. 2017, Space Sci. Rev., 207, 63

Willingale, R., Starling, R. L. C., Beardmore, A. P., Tanvir, N. R., & O'Brien, P. T. 2013, MNRAS, 431, 394

Wilms, J., Allen, A., & McCray, R. 2000, ApJ, 542, 914

Winkler, C., Courvoisier, T. J. L., Di Cocco, G., et al. 2003, A&A, 411, L1

Zhang, B., Fan, Y. Z., Dyks, J., et al. 2006, ApJ, 642, 354

Zhang, S. N., Feroci, M., Santangelo, A., et al. 2016, Society of Photo-Optical Instrumentation Engineers (SPIE) Conference Series, Vol. 9905, eXTP: Enhanced X-ray Timing and Polarization mission, 99051Q
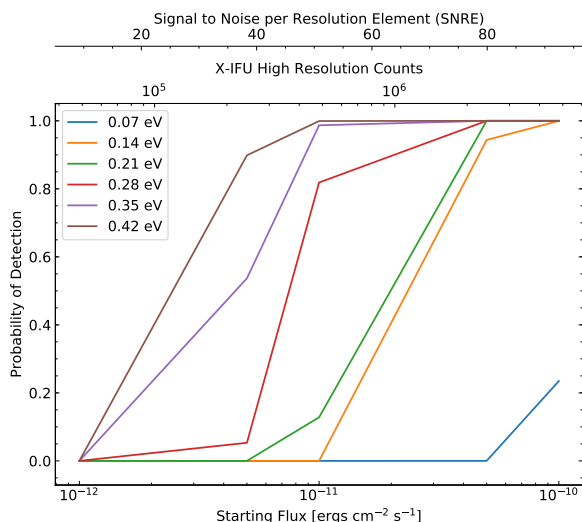
Fig. A.1: Detection probability of an unresolved absorption feature of a given equivalent width for GRB afterglow starting fluxes of 1, 5, 10, 50, and 100×10^{-12} erg cm^{-2} s^{-1}.

Appendix A: Predicting detection probability of the WHIM using Poisson statistics

The probability of detecting unresolved absorption features of Gaussian form within modelled astronomical spectra can be predicted using binomial statistics. The statistical significance required to detect a line of a given equivalent width EW is calculated by

$$\sigma = \frac{\text{EW} \cdot \Delta E}{\text{SNRE}}, \tag{A.1}$$

where $\Delta E = 2.5$ eV and SNRE is the signal-to-noise ratio per resolution element, which is calculated from the photon flux across the resolution elements in the energy range of the blind-line search. The binomial distribution determines the probability of detecting the absorption feature, out of N possible trials, for a one-sided probability associated with the σ value calculated using Eq. A.1.

Figure A.1 shows the probability of detecting an unresolved absorption feature of given equivalent width, in $N = 250$ redshift trials, for GRB afterglow starting fluxes of 1, 5, 10, 50, and 100×10^{-12} erg cm^{-2} s^{-1}. The detection probability presented in Sect. 4 are, on average, approximately a factor of 1.3 less than that of the theoretical results for a given equivalent width and starting flux of a GRB afterglow. The discrepancy between the detection probability from both methods could arise for a number of reasons. Firstly, the theoretical method predicts an ideal system in which instrument effects cannot easily be accounted for, such as the detector grading scheme or crosstalk between pixels, we assume a fully linear system, and we do not assume any additional spectral contribution, such as source background events. Secondly, the spectral binning and fit statistic chosen during the analysis can effect the detection of weak lines. Finally, the theoretical results cannot account for the interference of spectral edges on the detection of absorption features depending on their located redshift.